High-pressure behavior of synthetic mordenite-Na: an *in situ* single-crystal synchrotron X-ray diffraction study

Paolo Lotti[1*], G. Diego Gatta[1,2], Marco Merlini[1], Hanns-Peter Liermann[3]

[1]Dipartimento di Scienze della Terra, Università degli Studi di Milano, Via Botticelli 23, I-20133 Milano, Italy
[2]CNR – Istituto di Cristallografia, Sede di Bari, Via G. Amendola 122/o, Bari, Italy
[3]Photon Sciences, DESY, PETRA-III, Notkestrasse 85, D-22607, Hamburg, Germany

* Correspondence author: Paolo Lotti; e-mail: paolo.lotti@unimi.it; Tel: +39-02-50315609; Fax: +39-02-50315597

Abstract.

The high-pressure behavior of a synthetic mordenite-Na (space group: *Cmcm* or $Cmc2_1$) was studied by *in situ* single-crystal synchrotron X-ray diffraction with a diamond anvil cell up to 9.22(7) GPa. A phase transition, likely displacive in character, occurred between 1.68(7) and 2.70(8) GPa, from a *C*-centered to a primitive space group: possibly *Pbnm*, *Pbnn* or $Pbn2_1$. Fitting of the experimental data with III-BM equations of state allowed to describe the elastic behavior of the high-pressure polymorph with a primitive lattice. A very high volume compressibility [K_{V0} = 25(2) GPa, $\beta_{V0} = 1/K_{V0}$ = 0.040(3) GPa^{-1}; $K_V' = (\partial K_V/\partial P)_T$ = 2.0(3)], coupled with a remarkable elastic anisotropy ($\beta_b \gg \beta_c > \beta_a$), was found. Interestingly, the low-*P* and high-*P* polymorphs show the same anisotropic compressional scheme. A structure collapse was not observed up to 9.22(7) GPa, even though a strong decrease of the number of observed reflections at the highest pressures suggests an impending amorphization. The structure refinements performed at room-*P*, 0.98(2) and 1.68(7) GPa allowed to describe, at a first approximation, the mechanisms that govern the framework deformation in the low-*P* regime: the bulk compression is strongly accommodated by the increase of the ellipticity of the large 12-membered ring channels running along [001].

Introduction

Mordenite is a natural zeolite, commonly found in Nature in vugs of volcanic or intrusive rocks and as a diagenetic product of siliceous tuffs, with ideal composition: $(Na_2,K_2,Ca)_4[Al_8Si_{40}O_{96}]\cdot 28H_2O$ (Armbruster and Gunter, 2001; Passaglia and Sheppard, 2001). Its tetrahedral framework, *i.e.* MOR-type, shows a *Cmcm* topological symmetry and idealized unit-cell parameters *a* = 18.256, *b* = 20.534 and *c* = 7.542 Å (Baerlocher *et al*., 2007). The mordenite framework can be described with one secondary

building unit (SBU): the 5-1 SBU (Baerlocher *et al*., 2007). The [MOR]-framework type is built by sheets of six-membered rings of tetrahedra parallel to the (100) plane, linked to each other by four-membered rings of tetrahedra along [100] (Figure 1). This arrangement gives rise to two systems of channels running along the [001] direction (Figure 1): a large (6.5 x 7.0 Å, Baerlocher *et al*., 2007) twelve-membered ring channel (12mR[001]) and a highly compressed (2.6 x 5.7 Å, Baerlocher *et al*., 2007) eight-membered ring channel (8mR[001]). These channels are interconnected along the [010] direction by pockets accessible through 8mR[010] (3.4 x 4.8 Å, Simoncic and Armbruster, 2004) (Figure 1) and staggered by *c*/2 at the intersection with the 8mR[001] channels. In natural mordenites, the Si/Al-distrubution between the tetrahedral sites was found to be highly disordered. Extraframework cations are reported to occupy several positions: 1) in the pocket channels along [010], 2) centering the 12m- and 8mR[001] channels and 3) centering the 8mR[010] at the intersection between the 12mR[001] channel and the [010]-side pocket (Armbruster and Gunter, 2001). Although Na^+ is reported to be the main cationic constituent in natural mordenites, a highly variable extraframework chemistry, including samples with prevailing Ca^{2+} and K^+ and relatively high Mg^{2+}, Sr^{2+} and Ba^{2+}, has been found for several mordenites (Passaglia and Sheppard, 2001, and references therein).

The structure of mordenite was first refined by Meier (1961) in the centrosymmetric *Cmcm* space group. However, in this structural configuration a T-O-T intertetrahedral angle of 180° occurs, which is reported in the literature to be energetically unfavorable (*e.g*. Alberti *et al*., 1986; Armbruster and Gunter, 2001; Simoncic and Armbruster, 2004). Alberti *et al*. (1986) refined the mordenite crystal structure in the $Cmc2_1$ space group, which avoided T-O-T angles of 180°. Simoncic and Armbruster (2004) also refined the crystal structure of a natural and a synthetic mordenite-Na in the $Cmc2_1$ space group. However, they reported a strong *Cmcm* pseudosymmetry of the tetrahedral framework. Simoncic and Armbruster (2004) also reported the occurrence of a minor domain, in which all the framework sites are shifted by *c*/2, and proposed a structural model for the deformation of the 6mR-sheets to accommodate the interface between the two domains.

Beside the occurrence in Nature of exploitable deposits (*e.g.* Godelitsas *et al*., 2010), the synthetic counterparts of mordenite have also a large number of industrial applications: 1) as molecular sieves for gases (*e.g.* Delgado *et al*., 2006 and references therein), 2) as catalysts (*e.g.* Venuto, 1994; Vos *et al*., 2001 and references therein) or 3) as hosts for dye molecules (*e.g.* Simoncic *et al*., 2004; Simoncic and Armbruster, 2005; Deore *et al*., 2008 and references therein). In this light, the characterization of the mordenite behavior at different temperature and pressure conditions is necessary to describe its structure-related properties, to define its phase-stability fields and, possibly, new stable or metastable polymorphs. Several studies are available in the literature about the mordenite behavior at high temperature and the structural modifications in response to the dehydration process (*e.g*. Mortier *et al*., 1975; Schlenker *et al*., 1979; Elsen *et al*., 1987; Bish and Carey, 2001; Martucci *et*

al., 2003 and references therein). In particular, Martucci *et al*. (2003) studied the complex thermo-elastic behavior and dehydration mechanisms at the atomic scale of mordenite by *in situ* time-resolved synchrotron powder diffraction. On the other hand, very little is known about the high-pressure behavior of mordenite. Gatta and Lee (2006) performed an *in situ* synchrotron powder diffraction experiment, with a diamond anvil cell, on the synthetic mordenite-Na already studied at room conditions by Simoncic and Armbruster (2004). They reported the *P*-induced evolution of the unit-cell parameters and provided a description of the elastic behavior along with the refined elastic parameters. However, any attempt to perform crystal structure refinements at high pressure turned to be unsuccessful.
The finding of a single crystal large enough for an *in situ* high-pressure synchrotron diffraction experiment, from the same synthetic mordenite-Na prepared by Simoncic and Armbruster (2004) and studied by Gatta and Lee (2006), allowed us to further investigate the high-pressure behavior of this zeolite using a different experimental technique and a different *P*-transmitting medium. In particular, the aims of this study are: 1) to expand the knowledge on the high-pressure (and room-*T*) phase stability field of mordenite; 2) to describe the elastic behavior and compare the results with those of Gatta and Lee (2006); 3) to determine the *P*-induced structural modifications of mordenite at the atomic scale.

Sample and experimental methods

The mordenite-Na sample used for this study is the same already investigated at high pressure, by *in situ* synchrotron powder diffraction, by Gatta and Lee (2006) and synthesized by Simoncic and Armbruster (2004), who provided details about the synthesis protocol, chemical analysis and crystal structure determination by synchrotron single-crystal diffraction. The chemical formula, by electron microprobe analysis, reported by Simoncic and Armbruster (2004) is: $Na_6Al_{6.02}Si_{42.02}O_{96}\cdot 19H_2O$.
A single crystal (~ 40 x 30 x 30 μm^3), free of defects at the optical scale, was selected for the *in situ* synchrotron diffraction experiment at the Extreme Conditions Beamline P02.2 at PETRA/DESY, Hamburg, Germany. Further details on the beamline experimental setup are in Rothkirch *et al*. (2013) and Gatta *et al*. (2013). The crystal was loaded in a diamond anvil cell (DAC) with a 75° opening angle and equipped with Boehler-Almax-design diamond anvils. A steel foil (250 μm thick), serving as a gasket, was first pre-indented to ~ 70 μm and then drilled by spark-erosion in order to provide a pressure chamber (hole diameter = 175 μm). Few ruby spheres were also loaded into the DAC for pressure measurement by the ruby-fluorescence method (Mao *et al*., 1986; Chervin *et al*., 2001). A nominally anhydrous 4:1 methanol:ethanol mixture was used as hydrostatic *P*-transmitting medium (Angel *et al*., 2007). A total of 11 data collections was performed between 0.0001 (room-*P*, crystal in the DAC without *P*-medium) and 9.22(7) GPa, using an incident beam with energy of 42.8 keV (λ = 0.28968 Å). The same data collection strategy was adopted

for all the *P*-points: ω-rotation between -26 ≤ ω (°) ≤ +28 with 1° step scans. For the collections performed at P_0, P_1 (0.98(2) GPa) and P_2 (1.68(7) GPa), 1 second of exposure time per step was adopted, whereas between P_3 and P_{11} the exposure time was increased to 5 s per step. Diffraction data were collected with a Perkin Elmer XRD 1621 flat panel detector. Images were then converted into the "Esperanto" format using an in-house software script (Rothkirck *et al*. 2013) in order to be processed with the Crysalis software (Agilent, 2012).
Diffraction patterns from all the datasets have been indexed with an orthorhombic lattice, and unit-cell parameters have been determined by least-squares refinement based on Bragg reflections with 4.0 ≤ 2θ (°) ≤ 8.0. Data from P_0 to P_2 were compatible with the *Cmcm* (or $Cmc2_1$) space group, whereas diffraction data from P_3 to P_{11} clearly showed a phase transition from a *C*-centered to a primitive lattice along with a significant decrease in intensity. Intensity data reductions were performed using the Crysalis software (Agilent, 2012), applying corrections for Lorentz-polarization effects. A correction for the absorption by the DAC components was applied by scaling using the semi-empirical ABSPACK routine implemented in the Crysalis software (Agilent 2012). Data collected between P_3 and P_{11} showed a drastic reduction in the number of observed reflections ($I \geq 3\ \sigma(I)$) along with high R_{int} values (index of accordance between symmetrically related peaks). Structure refinements were then possible only with intensity datasets collected between P_0 and P_2. Refined unit-cell parameters between P_0 and P_{11} are reported in Table 1. Details pertaining to the intensity data collections and structure refinements between P_0 and P_2 are given in Table 2.

P-induced phase transition

The reflection conditions of the diffraction data collected between P_0 and P_2 are consistent with the *Cmcm* or the $Cmc2_1$ space group (Hahn, 2002), [see Simoncic and Armbruster (2004) for a thorough discussion on the presence of the inversion center]. Between P_2 and P_3 a strong decrease in the intensity of all the diffraction peaks, coupled with a consequent reduction of the number of observed reflections, was shown along with a significant number of diffraction spots violating the extinction rule for a *C*-centered lattice (*hkl*: $h + k = 2n + 1$, Figure 2). At higher pressures, the number and the intensity of reflections violating the *C*-centering increased, suggesting a phase transition from a *C*-centered to a primitive lattice. The analysis of extinctions from the datasets collected between P_3 and P_{11} clearly revealed the following systematic absences (Figure 2): 1) 0*kl*: $k = 2n + 1$; 2) *h*0*l*: $h + l = 2n + 1$. Due to the paucity of the experimental data, an unambiguous conclusion on the order of the phase transition cannot be drawn. Moreover, since a structure refinement of the primitive high-pressure polymorph cannot be carried out, a univocal space group assignment is not possible. However, we expect that the *P*-induced phase transition is displacive in character, as already observed for other open-framework compounds at

high pressure (*e.g.* Gatta *et al*., 2006, 2008, 2009, 2010). If a centric structure model is assumed for the low-pressure polymorph (with sp. gr. *Cmcm*), two primitive subgroups are consistent with the observed systematic extinctions previously reported: *Pbnm* (no. 62, setting *cab*; Hahn, 2002) and *Pbnn* (no. 52, setting *cab;* Hahn, 2002). The space group *Pbnn* can be recognized for the following systematic absences: *hk*0: $h + k = 2n + 1$. Unfortunately, the (*hk*0)* plane falls in the region shadowed by the DAC components (Figure 2), making an unambiguous assignment impossible. However, the reconstruction of the reciprocal plane (*hk*0)*, shown in Figure 2, shows the occurrence of at least one reflection with $h + k = 2n + 1$, which violates the space group *Pbnn*. In case an acentric structure model of the low-*P* polymorph is considered (*i.e*., with $Cmc2_1$), the observed extinctions suggest a transition to the $Pbn2_1$ subgroup (no. 33, setting *ba-c*, Hahn, 2002). We have derived the structure models of the high-*P* polymorph in the space group *Pbnm* and *Pbnn* (on the basis of the group-subgroup relationships and starting from the structure model of *Cmcm* mordenite refined at 1.68 GPa), but the quality of the intensity data of the high-*P* polymorph (*i.e.,* a drastic decrease of the intensities and, as a consequence, of the number of "observed" reflections) and the high number of variables to be refined made the refinements impossible.

Elastic behavior

The *P*-induced evolution of the unit-cell parameters *V*, *a*, *b* and *c* is reported in Table 1 and Figure 3. Although a continuous decrease in the intensity of the diffraction data was observed at the highest pressures investigated, a full amorphization of the high-pressure polymorph of the studied mordenite has been not observed up to 9.22(7) GPa.
Due to the very low number of experimental data preceding the phase transition, a fit with an equation of state was not possible for the low-pressure polymorph. The average volume and axial compressibilities in the ranges P_0-P_1, P_1-P_2 and P_0-P_2 have been calculated using the WINSTRAIN software (Angel, 2011) and are reported in Table 3. The softening observed along the *b*- and *c*-axes between 0.0001 – 1.68(7) GPa is likely ascribable to the impending phase transition.
The elastic behavior of the high-pressure primitive polymorph was described by fitting the experimental *V*-*P* data in the range P_3-P_{11} with a Birch-Murnaghan equation of state truncated to the third order (BM-III EoS, Birch, 1947; Angel, 2000) using the EoSFit7 software (Angel *et al*., 2014). The refined elastic parameters are: $V_0 = 2841(24)$ Å^3, $K_{V0} = 25(2)$ GPa and $K_V' = 2.0(3)$ (Figure 3). The evolution of the normalized pressure as a function of the Eulerian finite strain (F_e-f_e plot; Angel, 2000) is shown in Figure 3. A linear fit of the data corresponding to the range P_3-P_{11} was performed, leading to an intercept $F_e(0) = 25.3(5)$ GPa, in excellent agreement with the refined K_{V0} from the III-BM EoS fit. The negative slope of the F_e-f_e plot corroborates a refined $K_V' < 4$ (Angel, 2000).
The same strategy was adopted to describe the elastic be-

havior along the *a*, *b* and *c* crystallographic directions, by fitting the experimental data with "linearized" equations of state (Angel, 2000). The refined parameters [$K_{l0} = 1/3 \cdot \beta_l = (l/3) \cdot (\partial P/\partial l)$; $K_l' = \partial K_l/\partial P$] from fitting of the *b*-*P* data with linearized III-BM EoS are: b_0 = 21.2(4) Å, K_{b0} = 9(2) GPa and K_b' = 2.7(4). Due to the scattering and the high experimental uncertainties of the *a*-*P* and *c*-*P* data, as effect of the shadowing by the DAC components, the simultaneous refinement of three parameters led to an unstable III-BM EoS fit. II-BM EoS fit (K_l' = 4; Angel, 2000) led to unsatisfactory figures of merit. As a compromise, in order to get the best agreement between observed and calculated *l*-values, we performed a III-BM EoS fit by fixing K_a'= 3 and K_c'= 2.5, leading to the following refined values: a_0 = 18.18(5) Å and K_{a0} = 40(3) GPa; c_0 = 7.62(9) Å and K_{c0} = 23(4) GPa (Figure 3).

Structure refinements and *P*-induced framework deformation in the range 0.0001 – 1.68 GPa

The structure model of the low-*P* polymorph of the studied synthetic mordenite-Na was refined from the intensity data collected at P_0, P_1 and P_2, using the JANA2006 software (Petricek *et al*., 2014). Neutral X-ray scattering factors for Si, O and Na were taken from the *International Tables for Crystallography, Vol. C* (Wilson and Prince, 1999). The structure model of Simoncic and Armbruster (2004) was used as starting model. Simoncic and Armbruster (2004) reported an acentric $Cmc2_1$ space group, but with a strong *Cmcm* pseudosymmetry of the framework. In order to minimize the number of the refined parameters (to overcome the loss in the number of reflections for the shadowing due to the DAC components) and in consideration of the strong pseudosymmetry reported by Simoncic and Armbruster (2004), we adopted the *Cmcm* space group. Once the framework was modeled, an isotropic structure refinement was performed, using the Si scattering factor for all the T sites and restraining all the tetrahedral T-O bonds to 1.65(2) Å. The analysis of the difference-Fourier maps of the electron density allowed to locate the Na^+ and H_2O-oxygen sites within the elliptical 8mR[001] channels: Na1 and Ow1, respectively (Figure 4, Table 5). Further difference-Fourier syntheses allowed to locate several broad peaks in the 12mR[001] channel and in the 8mR[010] side pocket. However, the incomplete information for the limited portion of accessible reciprocal space did not allow to locate and refine the complex partially occupied and disordered extraframework population reported by Simoncic and Armbruster (2004). In the last refinement cycles, all the sites coordinates, the isotropic displacement parameters (U_{iso}) of the framework atoms, Na1 and Ow1 and their site occupancy factors (*sof*'s) have been simultaneously refined. In order to stabilize the refinement, the *sof*'s of all the other extraframework sites (*i.e.*, Na2-4 and Ow2-5, Table 5) have been fixed according to the residuals in the difference-Fourier maps of electron density, whereas their U_{iso} parameters have all been fixed to 0.08 $Å^2$. The same strategy was applied to the structure refinements at P_1 and P_2, start-

ing from the model obtained at P_0. All the refinements converged with no significant correlation between the refined parameters and with residuals in the difference-Fourier maps of electron density always $\leq \pm 1.1$ $e^-/Å^3$. The relatively high R_1 values (compared to the R_{int}) can be ascribed to the structural simplifications adopted in the refinements (mainly influencing the extraframework population), the influence of the DAC components on the intensity data and, overall, to the intrinsic structural complexity (with different domains coexisting in the same crystal; Simoncic and Armbruster, 2004). Statistical parameters on the structure refinements are listed in Table 2. Site coordinates, *sof*'s and U_{iso} parameters are given in Table 4, whereas relevant interatomic distances, angles and other structural parameters are in Table 5.

The crystal structure refinements from three pressure datasets allow a description, within experimental accuracy, of the deformation mechanisms of the mordenite framework in the range 0.0001-1.68(7) GPa. The bulk volume compression is significantly accommodated by the 12mR[001] channels, which strongly compress along both the O10-O10 (// *a*-axis) and the O7-O7 (// *b*-axis) diameters, leading to an increase of ellipticity (Figure 1; Table 5), which results in the highest compressibility along the *b* crystallographic axis (Table 3). On the contrary, the 8mR[001] channels are almost unaffected in the range 0.0001-1.68(7) GPa (Figure 1; Table 5), whereas the 8-membered rings $\perp$ [010] (giving access to the side pockets) undergo a slight compression with almost constant ellipticity (Figure 1; Table 5). Overall, the compression within the (100)-sheets is accommodated through the distortion of the puckered 6-membered rings of tetrahedra, *via* tetrahedral tilting, which is reported to be the main energetically convenient deformation mechanism in open-framework materials at high pressure (Gatta 2010). These sheets are linked along [100] by 4-membered rings, which do not accommodate the compression along the *a*-axis, given the slight lengthening of the O4-O4 diameter (Figure 1; Table 5). Along [100], the compression is accommodated by the side pockets linking the 12- and 8mR[001] channels, through the shortening of O3-O3 and O8-O8 (Figure 1 and Table 5).

Discussion

The high-pressure data obtained in this study show that the synthetic mordenite-Na undergoes a phase transition (probably displacive in character) from the *Cmcm* (or $Cmc2_1$) to the *Pbnm*/*Pbnn* (or $Pbn2_1$) space group, between 1.68(7) and 2.70(8) GPa. To the best of our knowledge, this transition was never reported in the open literature.

Although a description of the *P*-induced evolution of the extraframework components is not possible, the *P*-induced deformation of the tetrahedral framework can be described. Below the transition pressure, the bulk compression is strongly accommodated by the large 12mR[001] channels and by the [010]-side pocket voids.

A comparison of the compressional pattern of this study with that reported by Gatta and Lee (2006), for a powdered sample of the same material, clearly shows significant dif-

ferences. Gatta and Lee (2006) did not observe a clear evidence for a *P*-induced phase transition, even though they reported and commented a slight misfit between the calculated EoS and the experimentally observed compressional patterns at $P > 3$ GPa. Such a change in the compressional pattern was described as a potential change of the compressional mechanisms at high pressure. Beside this, Figure 3 clearly shows a remarkably different compressibility between the two samples, markedly higher for the high-*P* polymorph of mordenite of this study. The reasons for such a different behavior shown by the same starting material are still unclear. However, it is interesting to point out that two different *P*-transmitting fluids have been used in the two experiments: a 16:3:1 methanol:ethanol:water mixture by Gatta and Lee (2006) and a nominally anhydrous 4:1 methanol:ethanol mixture in this study. We cannot exclude that a *P*-induced overhydration occurred during the experiment performed by Gatta and Lee (2006), possibly promoted by the high surface area of the powdered sample (*e.g.*, Lee et al. 2002; Ori et al. 2008; Arletti et al. 2010). The extra H_2O molecules penetrated into the channels of the mordenite structure may act as a "filler" of the voids, making the structure less compressible. This kind of behavior was already observed in several zeolites compressed in "penetrating" and "non-penetrating" *P*-transmitting fluids (Gatta 2008, 2010; Gatta and Lee 2014). The free diameters of the mordenite framework allows the penetration of H_2O molecules. In addition, even the penetration of methanol and ethanol cannot be ruled out.

The description of the elastic behavior of the high-*P* polymorph by III-BM equations of state (Figure 3), shows a significantly anisotropic behavior. The refined elastic parameters reveal a drastic compressibility of the crystal structure along [010] (K_{b0} = 9(2)GPa and K_b' = 2.9(4)). In addition, the high-*P* primitive polymorph of mordenite exhibits a very high volume compressibility. The refined K_{V0} value [*i.e.*, 25(2) GPa)] is among the lowest so far reported for zeolites (Gatta, 2010), and significantly lower than that reported by Gatta and Lee (2006) for the *C*-centered structure of mordenite-Na (K_{V0} = 41(2) GPa, K_V' fixed to 4 from a II-BM EoS fit) studied up to 5.68 GPa. The anisotropic compressional scheme observed for the low- and high-*P* polymorph in this study and that reported by Gatta and Lee(2006) are all consistent with $K_{a0} > K_{c0} > K_{b0}$ (or $\beta_b > \beta_c > \beta_a$). The lack of structure refinements of the high-*P* polymorph prevents a discussion on the deformation mechanisms which drive the observed phase transition. However, the aforementioned compressional anisotropy can be intuitively explained with a compression of the 12mR[001] and 8mR[001] without any "inversion" in ellipticity (Figure 1). This implies a higher compressibility along [010] than along [100]. These findings corroborates the postulate of Gatta and Lee (2006): the open framework structures tend to accommodate the effect of pressure, by cooperative rotation of the tetrahedra, *usually* increasing the ellipticity of the channel systems and maintaining the original elliptical configuration, without any "inversion" in ellipticity.

Conclusions

The high-pressure behavior of the mordenite-Na synthesized by Simoncic and Armbruster (2004) was studied by means of *in situ* single-crystal synchrotron X-ray diffraction with a diamond anvil cell. A phase transition, likely displacive in character, occurred between 1.68(7) and 2.70(8) GPa, from the *Cmcm* (or $Cmc2_1$) to the *Pbnm*/*Pbnn* (or $Pbn2_1$) space group. Even if a clear picture cannot be drawn, very few data on the systematic absences on the (*hk*0)* plane suggest that the *Pbnn* space group may be discarded. Fitting of the experimental data with III-BM equations of state allowed to describe the elastic behavior of the high-*P* polymorph. The very high volume compressibility, coupled with a remarkable elastic anisotropy, suggests a metastable nature of the high-*P* polymorph, although a structure collapse was not observed at least up to 9.22(7) GPa. However, a strong decrease in the number of observed reflections at the highest pressures suggests an impending amorphization. The structure refinements performed at room-*P*, 0.98(2) and 1.68(7) GPa allowed to describe, at a first approximation, the mechanisms governing the framework deformation in the low-*P* regime, where the bulk compression is mainly accommodated by the 12mR[001] channels. Unfortunately, the *P*-induced structure deformation at the atomic scale of the high-*P* polymorph cannot be described for the lack of structure refinements.

The significant difference in the high-pressure compressional pattern of the synthetic mordenite-Na observed in this study and in that reported by Gatta and Lee (2006) from powder diffraction might be due to a *P*-induced overhydration effect experienced by the powder sample. However, the compressional anisotropy observed in this study for the low-*P* and high-*P* polymorph and that reported by Gatta and Lee (2006) are all consistent with the following scheme: $\beta_b > \beta_c > \beta_a$.

.

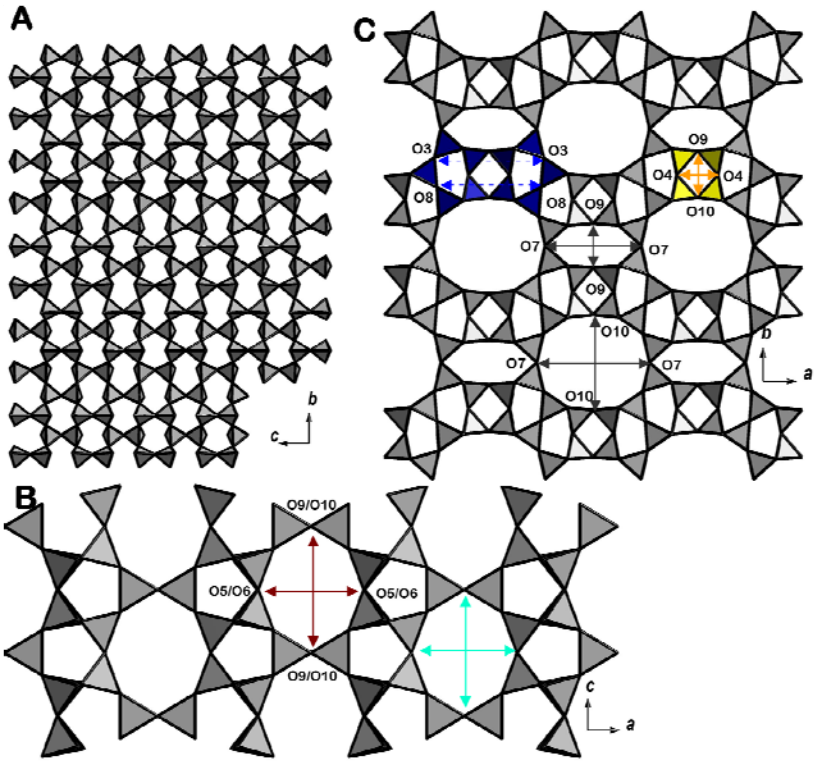

Figure 1. A) View of a puckered sheet of 6-membered rings of tetrahedra parallel to the (100) plane. B) The mordenite framework viewed down [010]. Two symmetrically-independent 8mR[010]'s occur. C) The mordenite framework viewed down [001]. One four-membered ring, connecting the (100)-sheets, and one [010]-side pocket are highlighted with different colors. Relevant structural parameters reported in Table 5 are shown in B) and C).

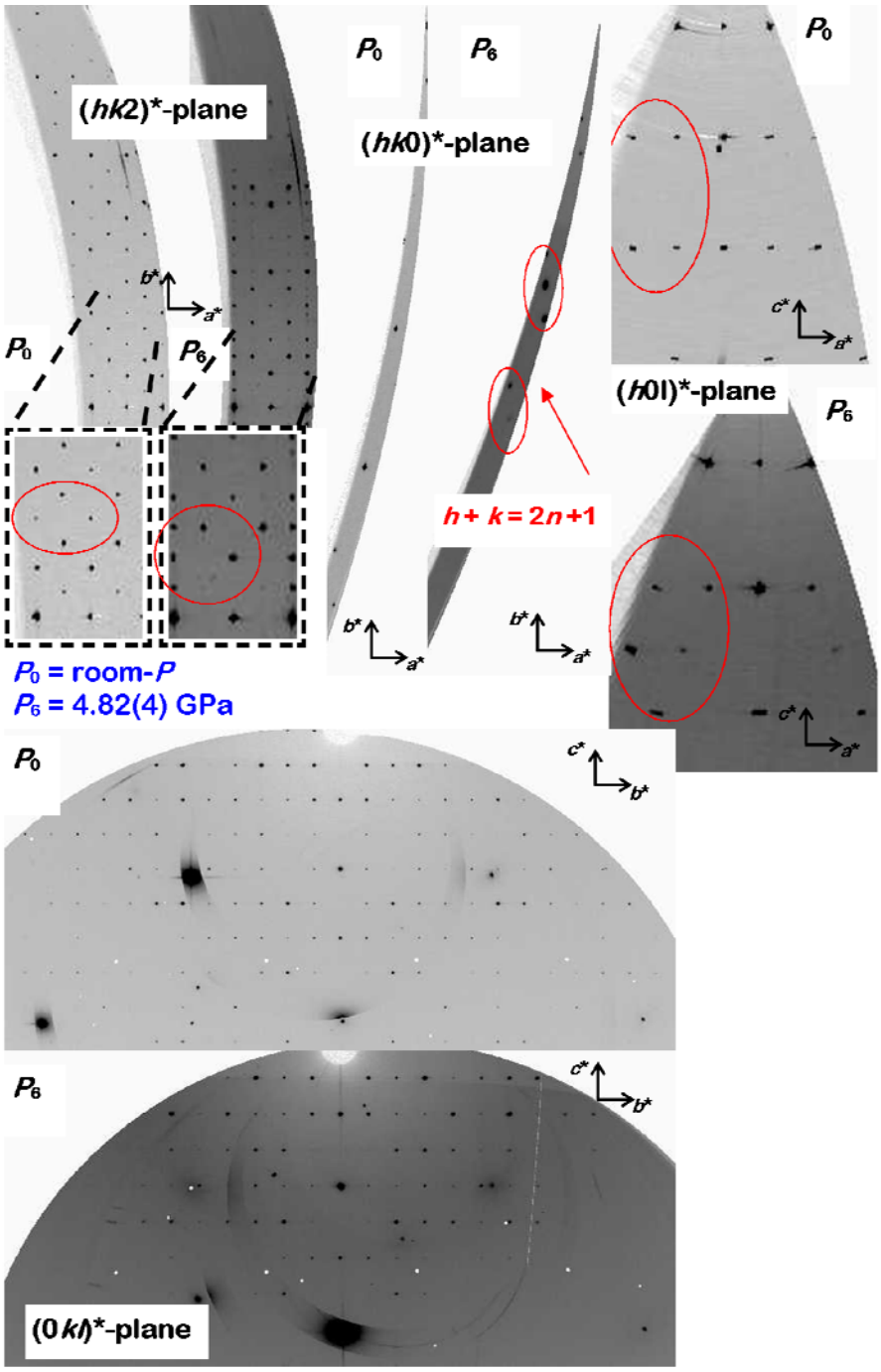

Figure 2. Reconstruction of the reciprocal lattice planes (*hk*2)*, (*hk*0)*, (*h*0*l*)* and (0*kl*)* at room-*P* (with a *C*-centered lattice) and 4.82(4) GPa (P_6, with a primitive lattice). Different systematic extinctions can be observed, inscribed in the circles. No change of the reflection conditions is observed on (0*kl*)*.

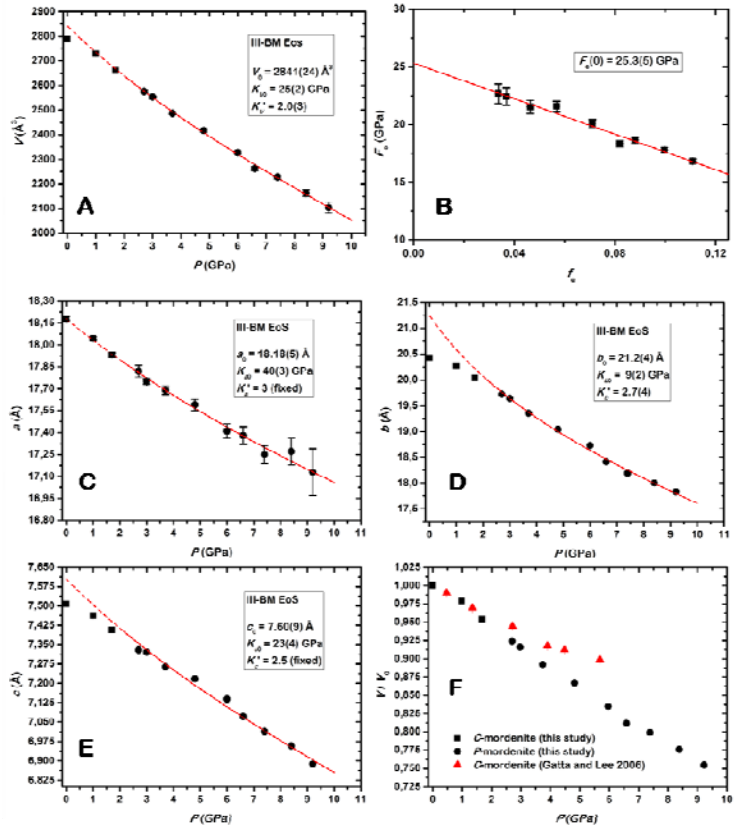

Figure 3. A) *P*-induced evolution of the unit-cell volume of mordenite. Square and round symbols refer to the *C*-centered and the primitive polymorphs, respectively. The III-BM EoS fit (on the data between P_3 and P_{11}) is shown. B) The normalized stress ($F_e = P/[3f_e + 2f_e)^{5/2}]$ *vs.* the Eulerian finite strain ($f_e = [(V_0/V)^{2/3} – 1)/2]$ plot (the III-BM-EoS-fit refined V_0 was used for calculations). The weighted linear fit through the data corresponding to the P_3-P_{11} range is shown. Estimated standard deviations have been calculated according to Heinz and Jeanloz (1984). C), D) and E) *P*-induced evolution of the *a*, *b* and *c* unit-cell parameters of mordenite, respectively. The "linearized" III-BM EoS fits (on the data between P_3 and P_{11}) are shown. F) *P*-induced evolution of the unit-cell volumes, normalized to the room-*P* values, from this study and from Gatta and Lee (2006).

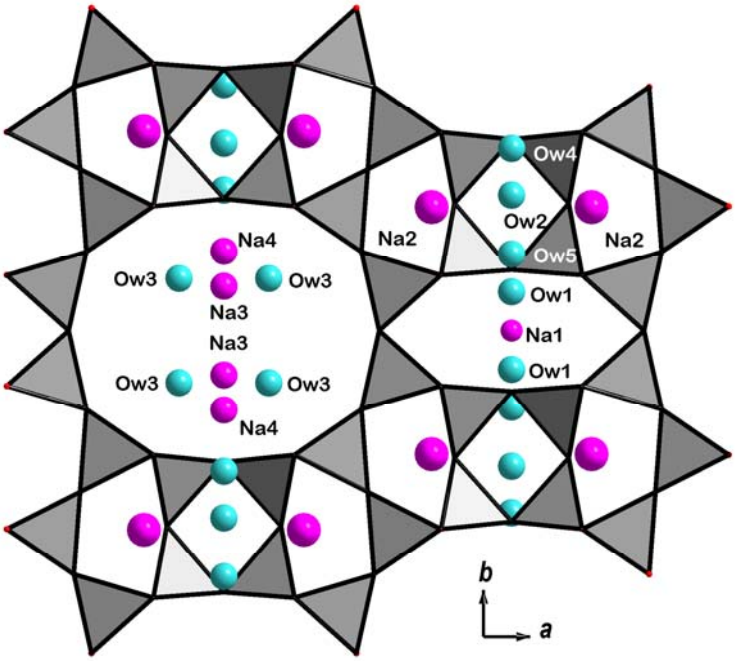

Figure 4. The extraframework population of the studied synthetic mordenite-Na at room-*P*, viewed down [001], as modeled from the analysis of the difference-Fourier maps of electron density.

Table 1. Unit-cell parameters of synthetic mordenite-Na at different pressures.

	P **(GPa)**	***a*** **(Å)**	***b*** **(Å)**	***c*** **(Å)**	***V*** **(Å^3)**
P_0	0.0001*	18.179(12)	20.4278(11)	7.5085(3)	2788(2)
P_1	0.98(2)	18.044(12)	20.2682(11)	7.4621(3)	2729(2)
P_2	1.68(7)	17.931(15)	20.0397(14)	7.4064(4)	2661(2)
P_3	2.70(8)	17.82(4)	19.723(4)	7.3290(11)	2576(6)
P_4	2.97(3)	17.75(2)	19.642(2)	7.3213(7)	2553(3)
P_5	3.74(5)	17.69(3)	19.352(3)	7.2638(9)	2487(4)
P_6	4.82(4)	17.59(4)	19.041(4)	7.2176(12)	2417(6)
P_7	5.96(6)	17.41(5)	18.728(5)	7.1391(15)	2328(7)
P_8	6.58(4)	17.38(6)	18.413(7)	7.072(2)	2263(9)
P_9	7.36(5)	17.25(6)	18.191(7)	7.014(2)	2228(9)
P_{10}	8.38(5)	17.27(9)	18.001(12)	6.958(3)	2163(13)
P_{11}	9.22(7)	17.13(16)	17.829(13)	6.888(5)	2104(22)

* Crystal in the DAC without *P*-medium

Table 2. Details pertaining to the intensity data collections and structure refinements of *C*-centered mordenite-Na at room-*P*, 0.98(2) and 1.68(7) GPa.

***P* (GPa)**	**0.0001 – P_0**	**0.98(2) – P_1**	**1.68(7) – P_2**
Maximum 2θ (°)	25.76	25.60	25.38
Measured reflections	3738	3540	3364
Unique reflections	774	755	743
Uinique reflections with $F_o > 3\sigma(F_o)$	592	502	488
R_{int}	0.0347	0.0540	0.0493
Number of l.s. parameters	59	59	59
R_1, $F_o > 3\sigma(F_o)$	0.0929	0.1130	0.1346
R_1, all data	0.1101	0.1445	0.1695
wR^2	0.1043	0.1167	0.1376
Residuals (e^-/Å^3)	+0.92	+1.07	+0.77
	-0.73	-0.76	-0.58

$R_{int} = \Sigma|F^2_{obs} - F^2_{obs}(mean)|/\Sigma(F^2_{obs})$; $R_1 = \Sigma(|F_{obs} - F_{calc}|)/\Sigma|F_{obs}|$;
$wR^2 = (\Sigma(w(F^2_{obs} - F^2_{calc})^2)/\Sigma(w(F^2_{obs})^2)^{0.5}$, $w = 1/(\sigma^2(F^2_{obs}))$.

Table 3. Average volume and linear compressibilities of the *C*-centered polymorph of synthetic mordenite-Na in the ranges P_0-P_1, P_1-P_2 and P_0-P_2, calculated using the WINSTRAIN software (Angel, 2011).

P-range	β_V (mean) (GPa^{-1})	β_a (mean) (GPa^{-1})	β_b (mean) (GPa^{-1})	β_c (mean) (GPa^{-1})
$P_0 - P_1$	0.022(5)	0.0076(10)	0.0079(4)	0.0063(3)
$P_1 - P_2$	0.036(14)	0.0089(17)	0.0160(16)	0.0106(11)
$P_0 - P_2$	0.027(4)	0.0081(7)	0.0113(3)	0.0081(2)

Table 4. Atomic fractional coordinates, site occupancy factors (*sof*) and isotropic displacement parameters (U_{iso}, Å^2) of the *C*-centered polymorph of synthetic mordenite-Na, refined at room-*P*, 0.98(2) and 1.68(7) GPa.

Site	*sof*	*x*	*y*	*z*	U_{iso}
			***P*$_0$ (0.0001 GPa)**		
T1	1.0	0.1967(3)	0.07317(8)	-0.0428(2)	0.0130(5)
T2	1.0	0.3032(3)	0.19012(8)	0.0452(2)	0.0136(4)
T3	1.0	0.0851(5)	0.1188(1)	0.25	0.0134(6)
T4	1.0	0.0860(5)	0.2747(1)	0.25	0.0146(6)
O1	1.0	0.1224(8)	0.0860(3)	0.0716(7)	0.036(2)
O2	1.0	0.1232(9)	0.3069(3)	0.0729(6)	0.033(2)
O3	1.0	0.2608(9)	0.1225(3)	0.0094(6)	0.040(2)
O4	1.0	0.100(2)	0.1972(4)	0.25	0.042(2)
O5	1.0	0.328(2)	0.1927(4)	0.25	0.031(2)
O6	1.0	0.175(1)	0.0782(4)	-0.25	0.027(2)
O7	1.0	0.230(1)	0	0	0.027(2)
O8	1.0	0.25	0.25	0	0.049(3)
O9	1.0	0	0.0947(8)	0.25	0.041(3)
O10	1.0	0	0.2957(7)	0.25	0.033(3)
Na1	0.68(4)	0	0	0	0.052(6)
Na2	0.13	0.142(7)	0.192(2)	-0.25	0.08
Na3	0.12	-0.5	-0.092(6)	0.25	0.08
Na4	0.24	0	0.379(2)	0.527(4)	0.08
Ow1	0.66(4)	0	0.059(2)	-0.25	0.074(11)
Ow2	0.56	0	0.206(2)	-0.25	0.08
Ow3	0.2	-0.421(8)	-0.093(3)	0.045(6)	0.08
Ow4	0.44	0	0.280(2)	-0.25	0.08
Ow5	0.36	0	0.118(3)	-0.25	0.08
			***P*$_1$ (0.98(2) GPa)**		
T1	1.0	0.1971(4)	0.0731(1)	-0.0431(3)	0.0176(6)
T2	1.0	0.3037(4)	0.1901(1)	0.0457(3)	0.0179(6)
T3	1.0	0.0853(6)	0.1186(2)	0.25	0.0168(8)
T4	1.0	0.0852(6)	0.2748(2)	0.25	0.0187(8)
O1	1.0	0.122(1)	0.0860(4)	0.070(1)	0.049(2)
O2	1.0	0.122(1)	0.3077(4)	0.0722(8)	0.042(2)
O3	1.0	0.261(1)	0.1223(4)	0.0137(9)	0.056(2)
O4	1.0	0.105(2)	0.1972(5)	0.25	0.058(4)
O5	1.0	0.333(2)	0.1952(6)	0.25	0.041(3)
O6	1.0	0.175(2)	0.0787(5)	-0.25	0.033(2)

O7	1.0	0.232(2)	0	0	0.035(2)
O8	1.0	0.25	0.25	0	0.075(5)
O9	1.0	0	0.097(1)	0.25	0.051(5)
O10	1.0	0	0.299(1)	0.25	0.046(5)
Na1	0.64(4)	0	0	0	0.049(7)
Na2	0.13	0.118(14)	0.187(4)	-0.25	0.08
Na3	0.12	-0.5	0.057(6)	0.25	0.08
Na4	0.24	0	0.385(2)	0.515(4)	0.08
Ow1	0.79(15)	0	0.061(2)	-0.25	0.11(3)
Ow2	0.56	0	0.205(3)	-0.25	0.08
Ow3	0.2	-0.416(9)	-0.071(3)	0.030(7)	0.08
Ow4	0.44	0	0.262(3)	-0.25	0.08
Ow5	0.36	0	0.121(4)	-0.25	0.08
			P_2 (1.68(7) GPa)		
T1	1.0	0.1959(5)	0.0735(1)	-0.0424(3)	0.0255(8)
T2	1.0	0.3042(5)	0.1904(1)	0.0460(3)	0.0274(7)
T3	1.0	0.0852(7)	0.1192(2)	0.25	0.024(1)
T4	1.0	0.0847(7)	0.2764(2)	0.25	0.026(1)
O1	1.0	0.119(1)	0.0847(6)	0.070(1)	0.069(3)
O2	1.0	0.122(1)	0.3086(5)	0.070(1)	0.064(3)
O3	1.0	0.262(1)	0.1222(6)	0.015(1)	0.087(4)
O4	1.0	0.106(2)	0.1974(6)	0.25	0.093(6)
O5	1.0	0.331(2)	0.1949(7)	0.25	0.055(4)
O6	1.0	0.176(2)	0.0787(6)	-0.25	0.040(3)
O7	1.0	0.235(2)	0	0	0.056(4)
O8	1.0	0.25	0.25	0	0.118(7)
O9	1.0	0	0.096(1)	0.25	0.065(7)
O10	1.0	0	0.303(1)	0.25	0.062(6)
Na1	0.70(5)	0	0	0	0.054(7)
Na2	0.13	0.132(15)	0.192(4)	-0.25	0.08
Na3	0.12	-0.5	-0.018(6)	0.25	0.08
Na4	0.24	0	0.391(2)	0.513(4)	0.08
Ow1	0.68(13)	0	0.058(2)	-0.25	0.09(3)
Ow2	0.56	0	0.205(2)	-0.25	0.08
Ow3	0.2	-0.424(9)	-0.066(3)	0.020(7)	0.08
Ow4	0.44	0	0.272(3)	-0.25	0.08
Ow5	0.36	0	0.106(4)	-0.25	0.08

Sof and U_{iso} parameters of Na2, Na3, Na4, Ow2, Ow3, Ow4 and Ow5 have been fixed. See the text for further details.

Table 5. Relevant interatomic distances (Å), inter-tetrahedral angles (°), channel diameters (Å) and ellipticities, from the structure refinements of the *C*-centered polymorph of synthetic mordenite-Na at room-*P*, 0.98(2) and 1.68(7) GPa.

			P_0 (0.0001 GPa)	P_1 (0.98(2) GPa)	P_2 (1.68(7) GPa)
T1-	O1		1.622(13)	1.625(17)	1.619(19)
	O3		1.590(13)	1.584(16)	1.59(2)
	O6		1.608(7)	1.598(9)	1.582(9)
	O7		1.645(9)	1.640(12)	1.659(14)
	<T1-O>		1.616	1.612	1.613
T2-	O2		1.606(15)	1.603(17)	1.586(19)
	O3		1.605(10)	1.593(13)	1.582(16)
	O5		1.601(8)	1.617(11)	1.588(11)
	O8		1.596(4)	1.590(5)	1.577(6)
	<T2-O>		1.602	1.601	1.583
T3-	O1	x2	1.644(9)	1.632(11)	1.625(13)
	O4		1.626(10)	1.630(13)	1.611(15)
	O9		1.623(10)	1.602(13)	1.600(15)
	<T3-O>		1.634	1.624	1.615
T4-	O2	x2	1.631(9)	1.627(11)	1.621(12)
	O4		1.604(10)	1.611(13)	1.629(15)
	O10		1.621(10)	1.616(12)	1.608(15)
	<T4-O>		1.622	1.620	1.620
	T1-O1-T3		147.2(5)	146.1(6)	143.2(8)
	T2-O2-T4		144.2(4)	143.2(5)	142.4(7)
	T1-O3-T2		160.0(5)	159.3(7)	157.9(10)
	T3-O4-T4		160.9(6)	155.1(7)	153.0(9)
	T2-O5-T2		147.73(8)	141.1(1)	144.1(1)
	T1-O6-T1		150.76(8)	150.1(1)	152.8(1)
	T1-O7-T1		136.68(8)	135.1(1)	130.4(1)
	T2-O8-T2		180	180	180
	T3-O9-T3		144.8(5)	147.9(5)	145.5(6)
	T4-O10-T4		144.3(5)	144.2(5)	141.7(6)
Na1-	O1	x4	2.886(12)	2.851(15)	2.780(17)
	O9	x2	2.696(12)	2.707(18)	2.66(2)
	Ow1	x2	2.233(18)	2.24(2)	2.19(2)
Na2-	O5		2.42(4)	2.55(12)	2.36(11)
	O6		2.40(5)	2.42(13)	2.40(11)

	O8	x2	2.96(9)	-	3.04(19)
	*Ow2		2.60(13)	2.16(25)	2.38(27)
	*Ow4		-	2.62(21)	2.86(23)
	*Ow5		2.99(12)	2.51(22)	2.93(23)
Na3-	O10		2.29(12)	-	-
	Ow3	x4	2.11(10)	2.60(10)	2.38(11)
	Ow3´	x4	-	-	2.95(11)
Na4-	O2	x2	2.78(3)	2.78(3)	2.80(3)
	O10		2.68(3)	2.63(4)	2.63(4)
	Ow4		2.62(5)	3.05(6)	2.96(6)
12mR[001]	#O10-O10		8.35(4)	8.12(6)	7.91(6)
	O7-O7		9.81(3)	9.68(4)	9.52(5)
	ε		0.851(6)	0.839(9)	0.830(10)
8mR[001]	#O9-O9		3.87(2)	3.93(3)	3.83(4)
	O7-O7		8.37(3)	8.37(4)	8.41(5)
	ε		0.462(6)	0.470(7)	0.456(9)
8mR[010]´	O5-O5		6.27(4)	6.03(5)	6.06(5)
	O9-O9		7.5085(3)	7.4621(3)	7.4064(4)
	ε		0.835(5)	0.808(5)	0.818(7)
8mR[010]´´	O6-O6		6.37(4)	6.32(5)	6.31(5)
	O10-O10		7.5085(3)	7.4621(3)	7.4064(4)
	ε		0.848(5)	0.847(7)	0.852(7)
4mR	O4-O4		3.65(4)	3.77(5)	3.80(5)
	O9-O10		4.11(2)	4.10(3)	4.15(4)
[010]-side pocket	O3-O3		9.48(2)	9.42(3)	9.39(3)
	O8-O8		9.090(6)	9.022(6)	8.966(8)

* Mutually exclusive bonds involved; # Calculated as the projections onto the (001) plane. Channel ellipticity ε = S/L, where S and L are the shortest and the longest diameters, respectively.

Acknowledgements: Petra Simoncic and Thomas Armbruster are thanked for the sample of synthetic mordenite-Na. Parts of this research were carried out at the light source PETRA III at DESY, a member of the Helmholtz Association (HGF). GDG and PL acknowledge the Italian Ministry of Education , MIUR Project: "Futuro in Ricerca 2012 – ImPACT-RBFR12CLQD". Two anonymous reviewers and the Editor W. Depmeier are thanked.

References

Agilent, *Xcalibur CCD System, Crysalis Software System*. **2012**

A. Alberti, P. Davoli, G. Vezzalini, *Z. Kristallogr.*, **1986**, *184*, 249-256.

R. J. Angel, Equations of state. *In: High-Temperature and High-Pressure Crystal Chemistry* (Eds. R. M. Hazen, R. T. Downs), Reviews in Mineralogy and Geochemistry, Vol. 41, p. 35-60. Mineralogical Society of America and Geochemical Society (Washington, DC) **2000**.

R. J. Angel, *Win_Strain Users Manual. A program to calculate strain tensors from unit-cell parameters.* http://www.rossangel.com, **2011**

R. J. Angel, M. Bujak, J. Zhao, G. D. Gatta, S. J. Jacobsen, *J. Appl. Cryst*., **2007**, ***40***, 26-32.

R. J. Angel, M. Alvaro, J. Gonzalez-Platas, *Z. Kristallogr*., **2014**, *229*, 405-419.

R. Arletti, S. Quartieri, G. Vezzalini, *Am. Mineral*., **2010**, *95*, 1247-1256.

T. Armbruster, M. E. Gunter, Crystal Structures of Natural Zeolites. *In: Natural Zeolites: Occurrence, Properties, Applications* (Eds. D. L. Bish, D. W. Ming), Reviews in Mineralogy and Geochemistry, Vol. 45, p. 1-68. Mineralogical Society of America and Geochemical Society, (Washington, DC) **2001**.

C. Baerlocher, L. B. McCusker, D. H. Olson, *Atlas of Zeolite Framework Types*, sixth ed., Elsevier, Amsterdam **2007**.

F. Birch, *Phys. Rev*., **1947**, *71*, 809-824.

D. L. Bish, J. W. Carey, Thermal Properties of Natural Zeolites. *In: Natural Zeolites: Occurrence, Properties, Applications* (Eds. D. L. Bish, D. W. Ming), Reviews in Mineralogy and Geochemistry, Vol. 45, p. 403-452. Mineralogical Society of America and Geochemical Society, (Washington, DC) **2001**.

J. C. Chervin, B. Canny, M. Mancinelli, *High Pressure Res*., **2001**, *21*, 302-314.

J. A. Delgado, M. A. Uguina, J. M. Gomez, L. Ortega, *Sep. Purif. Technol.*, **2006**, *48*, 223-228.

S. Deore, P. Simoncic, A. Navrotsky, *Micropor. Mesopor. Mat.*, **2008**, *109*, 342-349.

J. Elsen, G. S. D. King, W. J. Mortier, *J. Phys. Chem.*, **1987**, *91*, 5800-5805.

G. D. Gatta, *Z. Kristallogr.*, **2008**, *223*, 160-170.

G. D. Gatta, *Micropor. Mesopor. Mat.*, **2010**, *128*, 78-84.

G. D. Gatta, Y. Lee, *Phys. Chem. Minerals*, **2006**, *32*, 726-732.

G. D. Gatta, Y. Lee, *Mineral. Mag.*, **2014**, *78*, 267-91.

G. D. Gatta, F. Nestola, T. Boffa Ballaran, *Am. Mineral.*, **2006**, *91*, 568-578.

G. D. Gatta, N. Rotiroti, T. Boffa Ballaran, A. Pavese, *Am. Mineral.*, **2008**, *93*, 1588-1596

G. D. Gatta, N. Rotiroti, T. Boffa Ballaran, C. Sanchez-Valle, A. Pavese, *Am. Mineral.*, **2009**, *94*, 1137-1143.

G. D. Gatta, P. Lotti, M. Merlini, H-P. Liermann, M. Fisch, *J. Am. Ceram. Soc.*, **2013**, *96*, 2583-2592.

A. Godelitsas, P. Gamaletsos, M. Roussos-Kotsis, *Eur. J. Mineral.*, **2010**, *22*, 797-811.

T. Hahn, *International Tables for Crystallography. Volume A: Space-group symmetry*. Springer, Dordrecht **2002**.

D. L. Heinz, R. Jeanloz, *J. Appl. Phys.*, **1984**, *55*, 885-893.
Y. Lee, T. Vogt, J. A. Hriljac, J. B. Parise, J. C. Hanson, S. J. Kim, *Nature*, **2002**, *420*, 485-489.
H. K. Mao, J. Xu, P. M. Bell, *J. Geophys. Res.*, **1986**, *91*, 4673-4676.
A. Martucci, M. Sacerdoti, G. Cruciani, C. Dalconi, *Eur. J. Mineral.*, **2003**, *15*, 485-493.
W. M. Meier, *Z. Kristallogr.*, **1961**, *115*, 439-450.
W. J. Mortier, J. J. Pluth, J. V. Smith, *Mat. Res. Bull.*, **1975**, *10*, 1037-1046.
S. Ori, S. Quartieri, G. Vezzalini, V. Dmitriev, *Am. Mineral.*, **2008**, *93*, 1393-1403.
E. Passaglia, R. A. Sheppard, The Crystal Chemistry of Zeolites. *In: Natural Zeolites: Occurrence, Properties, Applications* (Eds. D. L. Bish, D. W. Ming), Reviews in Mineralogy and Geochemistry, Vol. 45, p. 69-116. Mineralogical Society of America and Geochemical Society, (Washington, DC) **2001**.
V. Petricek, M. Dusak, L. Palatinus, *Z. Kristallogr.*, **2014**, *229*, 345-352.
A. Rothkirch, G. D. Gatta, M. Meyer, S. Merkel, M. Merlini, H-P. Liermann, *J. Synchrotron Radiat.*, **2013**, *20*, 711-720.
J. L. Schlenker, J. J. Pluth, J. V. Smith, *Mat. Res. Bull.*, **1979**, *14*, 751-758.
P. Simoncic, T. Armbruster, *Am. Mineral.*, **2004**, *89*, 421-431.
P. Simoncic, T. Armbruster, *Micropor. Mesopor. Mat.*, **2005**, *81*, 87-95.
P. Simoncic, T. Armbruster, P. Pattison, *J. Phys. Chem. B*, **2004**, *108*, 17352-17360.
P. B. Venuto, *Microporous Mater.*, **1994**, *2*, 297-411.
A. M. Vos, X. Rozanska, R. A. Schoonheydt, R. A. van Santen, F. Hutschka, J. Hafner, *J. Am. Chem. Soc.*, **2001**, *123*, 2799-2809.
A. J. C. Wilson, E. Prince, *International Tables for Crystallography. Volume C: Mathematical, Physical and Chemical Tables*, 2nd ed., Kluwer, Dordrecht **1999**.